Special issue article

SURFACE and INTERFACE ANALYSIS

Received: 2 October 2015 Revised: 27 January 2016 Accepted: 3 March 2016 Published online in Wiley Online Library

(wileyonlinelibrary.com) DOI 10.1002/sia.6017

Spectroscopic investigation of nitrogen-functionalized carbon materials

Kevin N. Wood,[a,e] Steven T. Christensen,[b] Dennis Nordlund,[c] Arrelaine A. Dameron,[b] Chilan Ngo,[d] Huyen Dinh,[b] Thomas Gennett,[b] Ryan O'Hayre[a] and Svitlana Pylypenko[d]*

Carbon materials are used in a diverse set of applications ranging from pharmaceuticals to catalysis. Nitrogen modification of carbon powders has shown to be an effective method for enhancing both surface and bulk properties of as-received material for a number of applications. Unfortunately, control of the nitrogen modification process is challenging and can limit the effectiveness and reproducibility of N-doped materials. Additionally, the assignment of functional groups to specific moieties on the surface of nitrogen-modified carbon materials is not straightforward. Herein, we complete an in-depth analysis of functional groups present at the surface of ion-implanted Vulcan and Graphitic Vulcan through the use of X-ray photoelectron spectroscopy (XPS) and near edge X-ray adsorption fine structure spectroscopy (NEXAFS). Our results show that regardless of the initial starting materials used, nitrogen ion implantation conditions can be tuned to increase the amount of nitrogen incorporation and to obtain both similar and reproducible final distributions of nitrogen functional groups. The development of a well-controlled/reproducible nitrogen implantation pathway opens the door for carbon supported catalyst architectures to have improved numbers of nucleation sites, decreased particle size, and enhanced catalyst-support interactions. Copyright © 2016 John Wiley & Sons, Ltd.

Additional supporting information may be found in the online version of the publisher's web-site.

Keywords: Nitrogen; Carbon Support; Spectroscopy; catalysis; XPS; NEXAFS

Introduction

Carbon-based materials are among the most studied systems in the scientific community because of their versatility, low cost, availability, and a wide range of properties.[1–5] The physical, chemical, optical, and electronic properties of carbon materials vary among their allotropic forms and greatly depend on the structure, morphology, and surface composition of the carbon. High surface area carbon materials have been extensively used for sorption, sensing, catalysis, and storage applications. In many energy generation and storage applications, carbon materials are used as supports to facilitate dispersion of noble and non-noble catalysts. Among commercially available carbon supports, carbon blacks and activated carbons are the most commonly used, with various nanostructured carbons such as graphene, fibers, nanotubes, and mesoporous morphologies emerging in recent decades. Functionalization of these carbon-based materials allows researchers to tune carbons surface properties, increasing its utility across a wide range of applications.

In the case of carbon supports employed in catalytic processes, the most important characteristics are surface area, structural organization, porosity, and surface composition.[1] Synthesis and/or manufacturing routes often greatly influence the surface composition, leading to a range of concentrations for graphitic and oxide components.[2,5–7] Many different oxygen functional groups have been detected on carbon support materials including carboxyl, carbonyl, quinone, ether, hydroxyl, phenol, and lactone groups. These groups influence the acid/base nature of the support surface and act as nucleation centers during the deposition of metal catalysts.[2,8–10] In addition, the properties of carbon supports can be altered by the introduction of other heteroatoms, such as sulfur, phosphorous, boron, fluorine, iodine, and nitrogen.[3,11–14] Replacement of the carbon atoms with other heteroatoms changes local chemical reactivity, improving nucleation and enhancing binding energy between the support and metal nanoparticles.[15] Because of its size and the presence of a lone pair of electrons, nitrogen introduces defects into the carbon structure of graphitic carbon matrices.[2,4,5]

As a convincing body of recent work has shown, functionalization of the carbon support with heteroatoms is now widely regarded as one of the promising routes for improving the interactions between the support and noble-metal electrocatalysts for both reducing and oxidizing catalytic reactions in polymer electrolyte membrane fuel cell (PEMFC) applications.[2,3,16–19] Nitrogen

* *Correspondence to: Svitlana Pylypenko, Department of Chemistry and Geochemistry, Colorado School of Mines, 1012 14th Street, Golden, CO 80401, USA. E-mail: spylypen@mines.edu*

a *Department of Metallurgical and Materials Engineering, Colorado School of Mines, 1500 Illinois Street, Golden, CO, 80401, USA*

b *National Renewable Energy Laboratory, 15013 Denver West Pkwy, Golden, CO, 80401, USA*

c *Stanford Synchrotron Radiation Lightsource, SLAC National Accelerator Laboratory, 2575 Sand Hill Rd, Menlo Park, CA, 94023, USA*

d *Department of Chemistry and Geochemistry, Colorado School of Mines, 1012 14th Street, Golden, CO, 80401, USA*

e *Department of Mechanical Engineering, University of Michigan, Ann Arbor, MI, 48109, USA*

functionalization has also led to improvements in the nucleation of metal nanoparticles (NPs) when compared against unmodified references regardless of the type of carbon support used. The general trend among the literature reports indicates that increasing nitrogen levels tends to lead to decreased catalyst particle sizes.[14,16,20] However, nucleation is also enhanced by the presence of other defects such as carbon vacancies that can modify energy of adsorption and therefore improve nucleation.[17,21] Beyond nucleation effects, Density Functional Theory (DFT) calculations have indicated that energy of dissolution for metal catalysts can also be greatly affected by nitrogen defects, and whether the effect is beneficial or not depends on the functionality of the nitrogen and the nature of the metal catalyst.[22] Other DFT studies indicate that bonding between platinum and carbon increases in strength with the increasing number and proximity of nitrogen atoms. Recently, this has also been shown experimentally using electron energy loss spectral imaging (EELS) analysis to quantify nitrogen in the functionalized support on the nanometer length-scale and establish correlation between regions with high nitrogen content and stabilized metal nanoparticles.[22] More recent DFT work by Muhich *et al.* discusses the differences in behavior of nitrogen and boron functionalized graphene. Their results show that boron atoms have little influence on Pt atom migration outside the boron containing carbon rings, but can help trap Pt atoms. Meanwhile, nitrogen is less effective in preventing Pt atom hopping, but does increase the energy barrier, minimizing the migration of Pt atoms over nitrogen-containing sites and thereby improving the stability of Pt atoms up to 1 nm away from the nitrogen site.[23]

Chemical vapor deposition (CVD) and nano-casting from solution, followed by pyrolysis of precursor molecules, are perhaps the most popular routes to incorporate nitrogen functionalities into the bulk of carbon materials.[4,24,25] However, substitutional doping of graphene can also be achieved with other direct synthesis routes such as segregation growth and solvothermal approaches. Synthesis of N-containing nanotubes, nanofibers, and graphene is typically aimed at increasing the amount of nitrogen incorporation and forming specific functionalities and bonding environments, which can be controlled by the growth parameters. Between the low and high doping regimes that exist in this synthesis, the latter is recognized as experimentally challenging.[2] While there are many analogies between nitrogen-modified bulk carbons and nanostructures with well-defined dimensions, one must use caution comparing the two systems.[5]

In addition, post-synthesis routes including thermal treatment and ion implantation have been studied as possible methods for modifying the surface layer of carbon supports. Studies of nitrogen implanted highly ordered pyrolytic graphite (HOPGs) allow for the basic understanding of nitrogen implanted functionalities while reducing the complexity/heterogeneity associated with the incorporation of nitrogen into high surface area carbons.[18,26] Because ion implantation not only incorporates nitrogen but also creates structural damage, studies have compared unmodified and N-modified HOPG to HOPG modified with Ar. These studies demonstrated the negative effects of edge defects and vacancies present in Ar modified samples.[17,21] Low implantation dosages of nitrogen also resulted in significant physical damage and incorporation of only small amounts of nitrogen, causing a negative effect on the stability of noble metal catalyst nanoparticles. However, at higher implantation dosages, a significant amount of nitrogen was incorporated achieving saturation levels for both physical damage and nitrogen concentration (~6–8%). Various types of nitrogen functionalities were detected on the surface of modified HOPG, indicating that implantation results in the incorporation of nitrogen into the graphitic network via the formation of graphitic-type nitrogen, as well as the increase of edge-plane sites through the formation of doubly coordinated nitrogen species. It was hypothesized that high implantation dosages led to the formation of clustered multi-nitrogen defects, which led to improved durability of the supported metal nanoparticles.

Several research groups have applied ion implantation to modify higher surface area materials, including Carbon Nanotubes (CNTs) and carbon blacks. While incorporation of nitrogen into CNTs has been most widely studied using chemical methods, Xu *et al.* have demonstrated CNTs modified with nitrogen implantation. Their work explored 3 keV ion implantation producing nitrogen concentration in the range of 1.5–11.3 at% while also studying the effect of post annealing. The results showed triangular sp^2 and tetrahedral sp^3 configurations at lower temperatures and preferential substitutional nitrogen after higher annealing temperatures. In the case of carbon blacks, ion implantation was performed using 100 eV and resulted in about 1–2 at% nitrogen, leading to improved PtRu catalyst durability.[22,27–29]

While some effort has been placed on understanding the role of nitrogen in realistic 'application-based' environments utilizing high surface area carbon supports, a lack of knowledge exists in understanding the specific nitrogen functionalities and their role in improving performance.[30] In this work, we expand the understanding of nitrogen-functionalized high surface area carbon supports by focusing on the careful analysis of the distribution of nitrogen functionalities through XPS and NEXAFS, created using a variety of ion implantation parameters. The results contained herein show that increasing implantation time only marginally elevates nitrogen concentration, forming mostly single defect structures. Increasing the beam current results in the formation of more complex defect structures containing clustered multi-nitrogen defects, similar to those observed in carbon nitride materials. We also show that higher nitrogen dosage levels create a more homogeneous distribution of nitrogen functionalities, regardless of the initial carbon material or the resulting nitrogen concentration.

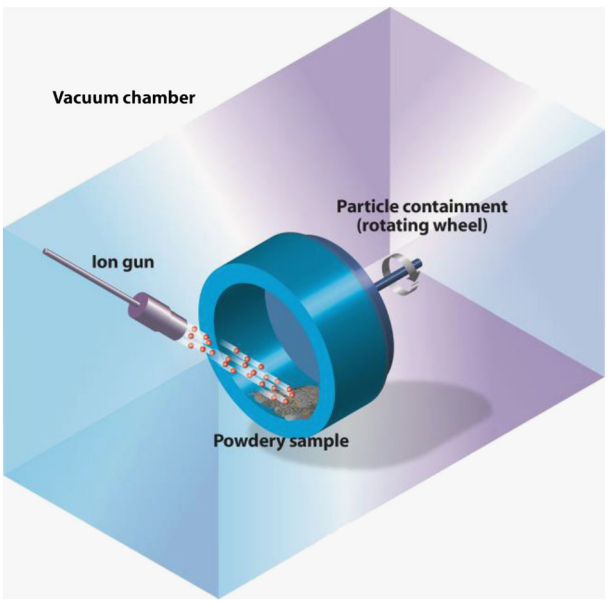

Figure 1. Schematic of vacuum chamber for the ion implantation of high surface area carbon materials.

SURFACE and INTERFACE ANALYSIS

Experimental

Nitrogen implantation of powder carbon samples was performed in a custom chamber[31] using an ion source. The chamber featured a rotating wheel (rotated at 30 rpm) to ensure more homogeneous functionalization of powder materials (Fig. 1). During an experiment, a standard mass (500 mg) of commercially available powder (Vulcan, Graphitic Vulcan, Ketjenblack, Graphitic Ketjenblack, MSC-30, PEEK, and Black Pearl) was put into the rotating sample holder (Fig. 1), and the chamber was evacuated to less than 5×10^{-6} Torr. Prior to implantation, the carbon powders were out-gassed by heating to above 180 °C for 15 min and then implanted with a 3 cm direct current (ITI) Ion Source (Veeco) at a pressure of 1×10^{-3} Torr (N_2) using a range of beam currents and implantation times. After implantation, the samples were slowly brought back to standard pressure using N_2 gas and exposed to atmospheric conditions. For more experimental details on the implantation process, we refer readers to Reference 30.

X-ray photoelectron spectroscopy analysis was performed on a Kratos Analytical Ltd, Manchester, U.K. (Kratos Nova X-ray photoelectron spectrometer) using a monochromatic Al Kα source operating at 300 W, while providing charge compensation using low-energy electrons. Survey and high-resolution C1s, N1s, and O1s spectra were acquired at 160 eV and 20 eV, respectively, for at least three areas per sample. Spectra were analyzed and quantified using CasaXPS software employing sensitivity factors supplied by the manufacturer. Analysis included the subtraction of a linear background and charge referencing to the aromatic carbon signal at 284.8 eV. Spectra were fitted with a series of 70% Gaussian/30% Lorentzian line shapes with a width constrained to 0.9–1.2 eV.

Near edge X-ray adsorption fine structure spectroscopy data were collected at beamline 10-1 of the Stanford Synchrotron Radiation Lightsource (SSRL), SLAC National Accelerator Laboratory in Menlo Park, California. Beamline 10-1 uses a spherical grating and a wiggler insertion device with a spot size of $<1\,mm^2$. The light source has a linear polarization of ~80% and an energy resolution ($\Delta E/E$) greater than 2×10^{-4}. The endline analysis chamber has an operating vacuum pressure of ~10^{-9} Torr and is equipped with a cylindrical mirror analyzer Phi Sciences Inc., Cottonwood, Arizona, USA (CMA, PHI, Inc.), a Channeltron total electron yield detector, and an XYZ sample control translation stage, which also provides rotational command. Data was collected while monitoring the beam flux with a gold mesh as well as a reference sample of mixed metal oxides.

The incoming flux was normalized by monitoring the beam flux with a gold mesh mounted upstream of the main chamber. The slits of the monochromator were opened to provide intermediate energy resolution (<0.2 eV) in the NEXAFS, and in the XPS measurements, the CMA analyzer was operated at 50 eV pass energy for a resolution of about 0.5 eV (~0.7 eV total). The energy scale of the

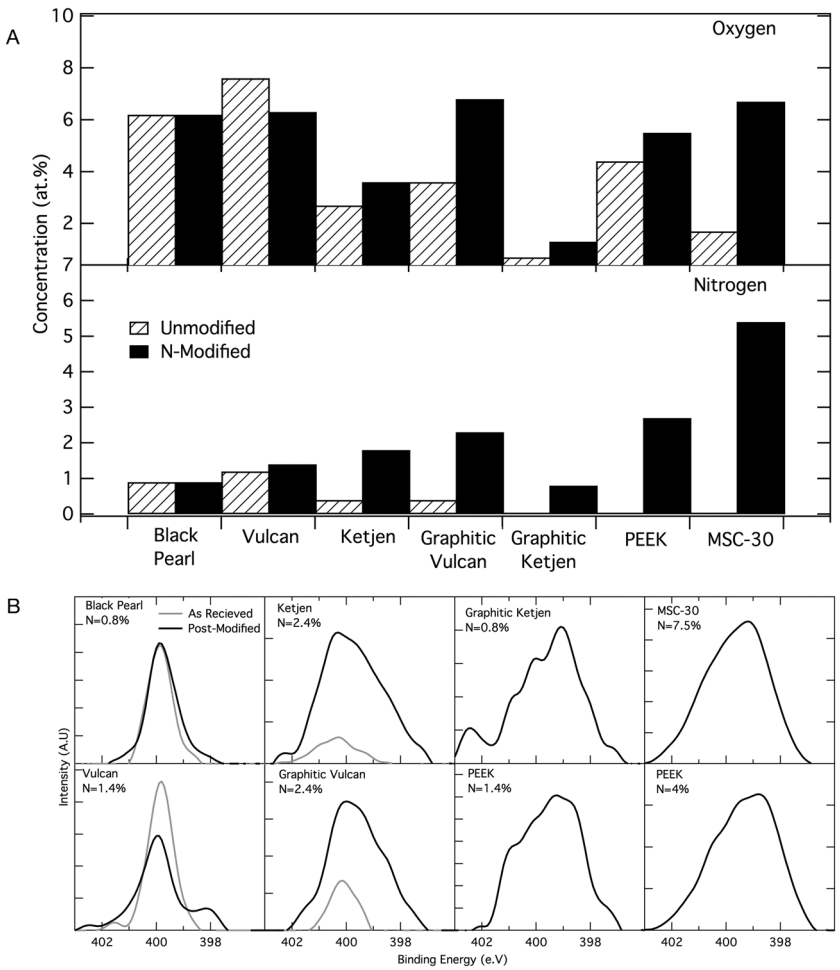

Figure 2. (A) Surface concentration of nitrogen and oxygen in pre-implanted and post-implanted carbon materials, atomic % and (B) XPS high-resolution N1s spectra of pre-implanted and post-implanted carbon materials.

NEXAFS scans was calibrated by first correcting monochromator energy drifts by simultaneous collection of a reference spectra from a calibration sample intercepting a few percent of the beam upstream of the main chamber, IREF(E), for all scans. The absolute energy scale was then determined by comparison to a boron nitride reference standard calibrated according to Jimenez *et al.*[32]

Results and discussion

Low-dosage implantation: commercial carbons

To examine the effects of nitrogen on various commercially available carbon materials, ion implantation was completed using the identical implantation conditions for each of the carbon materials listed in the Experimental section. The ion implantation current was set at 13 mA and for a period of 60 min ('low-dose' conditions) while the powder was 'tumbling' in the rotating wheel of the implantation chamber. Each powder was analyzed with XPS before and after implantation. The concentrations of oxygen and nitrogen before and after low-dose implantation, shown in Fig. 2, do not reveal any clear trends between the initial and final elemental compositions. High-resolution N 1s spectra, shown in Figure 2b, reveal that the N-functionalities present in the doped carbons depend strongly on the nature of the initial carbon material. However, the functionalities present after doping are not related to the initial surface composition measured with XPS (Figure 2a) or the level of graphiticity estimated from Raman analysis (SI Fig. 1). The scanning electron microscopy (SEM) images provided in Supporting Information Fig. 2 also do not show a clear trend between morphology type and N-doping concentration. In other words, the implanted nitrogen content under low-dose conditions is likely influenced by a wide range of surface-specific properties (e.g. porosity, surface area, morphology, graphiticity, and level of oxidation).

Based on these results, it is likely that 'low-dose' conditions lead to single defect sites, which are highly dependent on the initial properties of the carbon. Therefore, we examined implantation using higher dosages for selected materials to determine if more extensive implantation could lead to improved control and reproducibility of the resulting nitrogen surface functionalities. Vulcan and Graphitic Vulcan were selected for the 'high-dosage' study because they showed dramatically different behavior when implanted under 'low-dosage' conditions (Fig. 2B). The selection of Vulcan and Graphitic Vulcan was also motivated by the strong differences in the behavior of these materials when used as supports for precious metal catalysts in PEMFCs. Specifically, while graphitization of supports has been shown to lower carbon corrosion, these corrosion resistant supports have a low density of nucleation sites (resulting in poor dispersions of the Pt NPs and poor Pt/support interactions). By incorporating favorable surface functional groups through controlled doping, this issue can be addressed, providing significant enhancement while still enabling the use of a traditional, low-cost carbon material.

Table 1 lists implantation conditions and the resulted dosage levels supplied to the Vulcan and Graphitic Vulcan powder samples discussed in the remainder of this work.. Dosage levels are given in total ions delivered by the beam rather than ions/cm^2 because of uncertainly in the true surface area exposed during implantation of powder samples.

Table 1. The number of ions reaching the surface of the various carbon powders for each implantation condition. 13 mA/60 min was used as the baseline 'low-dose' condition

Beam current (A)	Implant time (min)	Implant time (s)	Charge (C)	Dosage (ions × 10^{20})
0.013	20	1200	15.6	0.97
0.013	45	2700	35.1	2.2
0.013	60	3600	46.8	2.9
0.013	90	5400	70.2	4.4
0.022	60	3600	79.2	4.9
0.013	120	7200	93.6	5.8
0.035	60	3600	126	7.8
0.05	60	3600	180	11.2

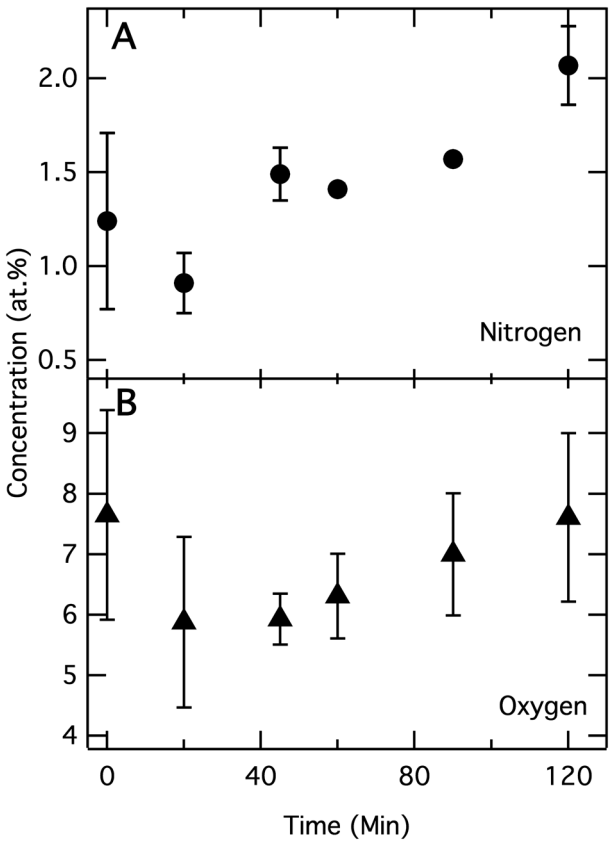

Figure 3. Atomic concentration of (A) nitrogen and (B) oxygen in Vulcan as a function of implantation time at constant implantation beam current ≈ 13 mA. The balance is carbon (i.e. for sample prior to implantation (Time = 0), elemental composition is N = 1.25%, O = 7.75%, and C = 91%).

Implantation time series: Vulcan

To explore the effect of the implantation time, Vulcan black was implanted for a range of times from 0 to 120 min at a constant beam current of 13 mA. Two regimes can be seen in Fig. 3, which plots the concentration of nitrogen and oxygen as a function of implantation time (0–20 min decreasing functionalization and 40–120 min increasing functionalization). On average, undoped Vulcan contained 1–1.5 at% nitrogen and 7–9 at% oxygen. Carbon blacks typically have different oxygen functional groups on the support surface (i.e. carboxyl, quinone, ether, etc.). The N1s XPS of unmodified Vulcan (Fig. 4A) shows a relatively narrow peak at a binding energy (BE) of 399.8 eV (N_o). This binding energy is commonly observed in nitrogen-containing polymers reporting C–N and/or O = C–N types of functionalities.[33] This range can also be attributed to

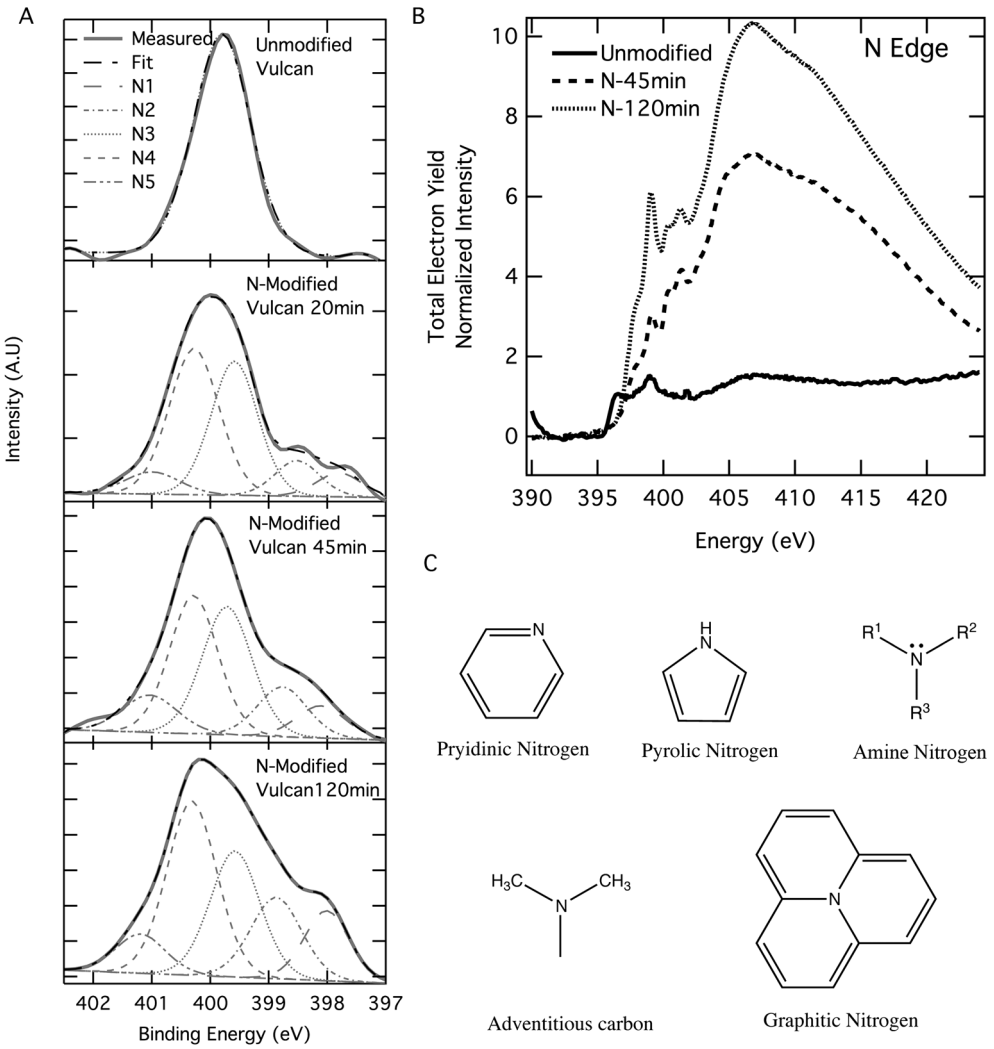

Figure 4. Characterization of the Vulcan as a function of implantation time at constant implantation beam current ≈ 13 mA. (A) XPS high-resolution N1s spectra, (B) NEXAFS N K edge, and (C) chemical structures of possible nitrogen functionalities. NEXAFS, near edge X-ray adsorption fine structure spectroscopy.

chemisorbed nitrogen species.[34] Therefore, we ascribe the detected nitrogen in undoped Vulcan to either impurities during the synthesis of the carbon or to chemisorbed N-species from atmospheric conditions.

During the initial stage of implantation on Vulcan, the concentration of nitrogen species is depleted. In Fig. 3A, the nitrogen content is reduced by a factor of 2 after only 20 min, confirming that a large number of nitrogen surface groups are very weakly bound to the carbon and easily removed. After 20 min of implantation, the initial peak observed in the high-resolution scan of unmodified Vulcan is no longer observed. Instead, five new peaks are positioned at 398 (N1), 398.8 (N2), 399.6 (N3), 400.3 (N4), and 401 eV (N5). The formation of these new species is commensurate with the relative decrease in the total nitrogen content and indicates that new nitrogen defects are created while the initial weakly bonded species are removed ('regime 1'). As implantation time increases beyond 20 min ('regime 2'), the total nitrogen concentration as well as the concentration of newly formed functionalities increases. At higher dosage levels, the nitrogen content exceeds 2 at% with a distinctive increase in N4, N1, and N2.

During the initial 20 min of implantation, the overall concentration of oxygen decreases (Fig. 3B). Compared with nitrogen however, fewer oxygen species are removed during the initial 20 min of implantation, resulting in an increase in the oxygen/nitrogen ratio. The remaining oxygen species are associated with well-defined, chemically incorporated oxygen surface groups, as has been previously mentioned. As the implantation time increases beyond 20 min, the variability of the oxygen concentration between various areas of the sample gradually decreases, while the overall oxygen content starts to increase, suggesting the creation of surface defects during implantation that are passivated/oxidized by oxygen species upon subsequent exposure of the sample to atmosphere.

To help identify the nitrogen species formed during ion implantation, we correlate XPS and NEXAFS spectral scans measured after the different implantation times (Fig. 4). Throughout the literature, there are three BE regions identified for major functional groups in nitrogen-doped carbon materials, graphitic nitrogen, pyridinic nitrogen, and pyrrolic nitrogen.

For XPS, structures that have nitrogen substituted for carbon (graphitic nitrogen) are typically reported between 399.8 eV and 401.8 eV.[30,35] In Fig. 4, N4 (400.3 eV) is the most dominant XPS peak after implantation, which falls within the region for graphitic or substitutional nitrogen. This binding energy is slightly lower than

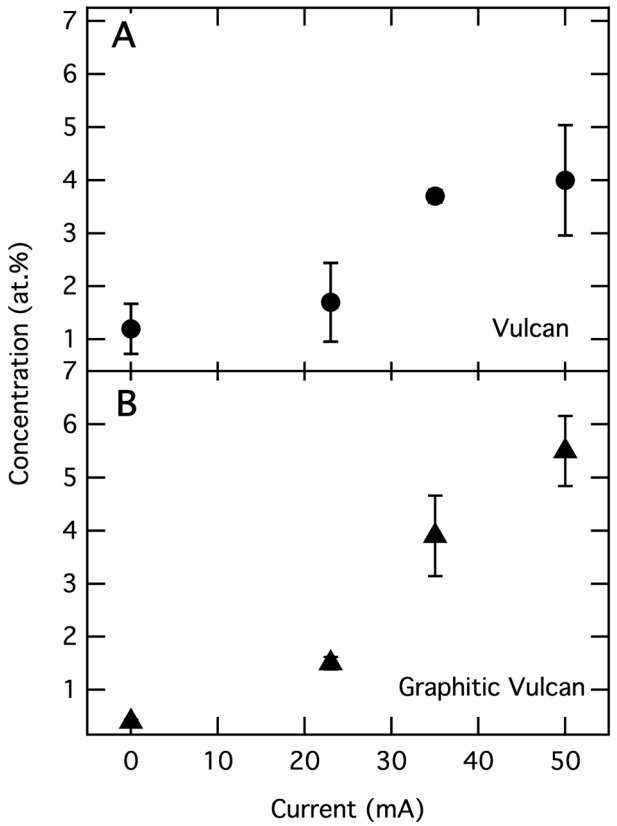

Figure 5. Nitrogen concentration shown for (A) Vulcan and (B) Graphitic Vulcan as a function of implantation beam current and constant implantation time of 60 min per sample.

the binding energy reported for azafullerenes; molecules that contain a *single* nitrogen substitution (400.7 eV). Additionally, we observe a small XPS peak at 401.2 eV (N5) that could also be ascribed to graphitic/substitutional nitrogen, similar to those observed by others in CVD-synthesized and ion-irradiated graphene materials.[30] The wide range of BE's reported for graphitic/substitutional N have been attributed to differences in the core hole screening, substrate effects, and different structural orders.[30] Because of this wide BE range, Peak N4 could also have contributions from species, such as amide groups (N–C = O).[36] The correlation between the increased relative intensity of N4 and the increased amount of oxygen species (Fig. 3) as implantation time increases supports this assignment. However, NEXAFS provides another clue into the convoluted identity of N4. The NEXAFS signature at ~400.5 eV (Fig. 4B) likely corresponds to the low-energy pi star resonance from a 3-coordinated nitrogen site,[30,37–39] indicating the presence of graphitic nitrogen in these samples. Therefore, a combination of graphitic and amide-like functional groups is expected.

In nearly all studies on N-doped carbon supports, low BE XPS peaks located near N2 are typically assigned to pyridinic nitrogen.[26,40–43] The NEXAFS data shows a strong resonance at 398.8 eV, which could be associated with either pyridinic nitrogen or other high-density nitrogen defect structures like triazine.[44] The XPS and NEXAFS features associated with these types of structures increase in relative intensity as implantation dose increases, indicating that clustered nitrogen defect sites increase with implantation time. This hypothesis is further confirmed by the increasing intensity of peak N1, located at 398.0 eV, which likely corresponds to the sp^2 nitrogen in imine-like functional groups.[45]

For the entire sample set shown in Fig. 4, the XPS peak at 399.6 eV (N3) appears in relative abundance; however, the assignment of this peak is not straightforward, as many functionalities,

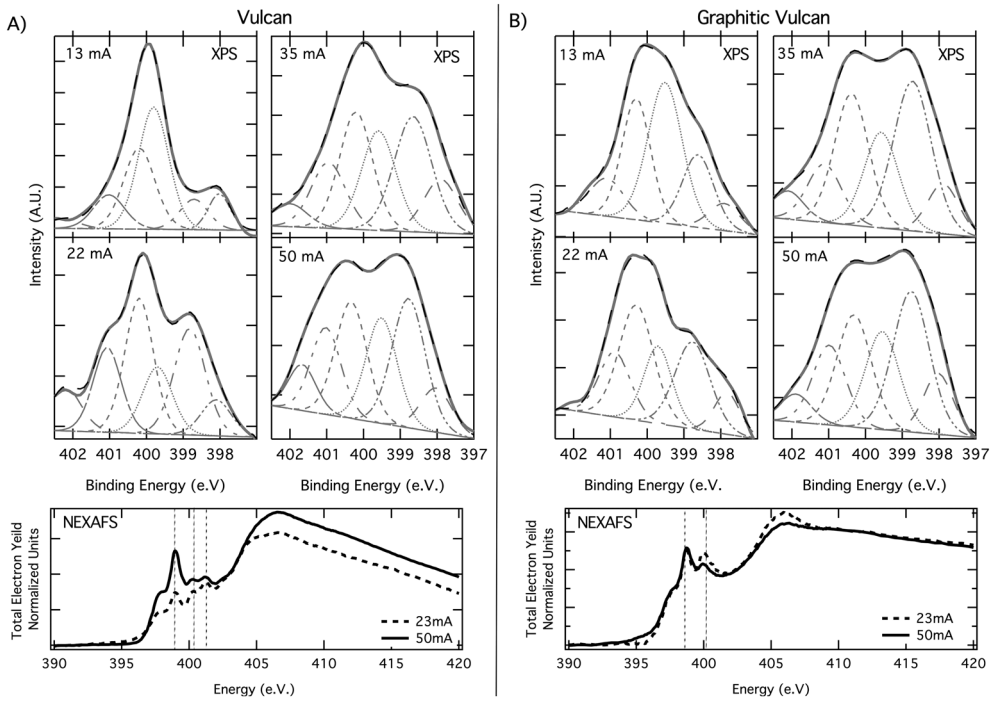

Figure 6. XPS and NEXAFS characterization of (A) Vulcan and (B) Graphitic Vulcan as a function of beam current and a constant implantation time of 60 min. NEXAFS, near edge X-ray adsorption fine structure spectroscopy.

including pyrrole, nitrilic, and amine, have been reported in this energy range.[2,18,30,46,47] As such, we are using NEXAFS to help elucidate the dominant functionality present in this BE range for our samples. In NEXAFS, a 1 s -> pi star transition is expected at ~402.3 eV for pyrrolic nitrogen[48,49]; however, the samples examined here do not possess a spectral feature at this energy. Additionally, the imprint of nitrilic species near 399.6 eV is not observed in our NEXAFS data either.[50–53] Therefore, we conclude that the XPS peak N3 cannot be attributed to pyrrolic or nitrilic species. Combining this insight with the appearance of a well-defined NEXAFS peak around 401.2 eV, it is most possible that N3 is associated with amine-like functional groups.[54,55]

In total, Fig. 4 shows the general trends for the nitrogen functionalities as a function of implantation time in Vulcan. After the nitrogen-cleaning phase of 20 min, we observe the nitrogen peaks N1 (imine), N2 (pyridinic), N3 (amine), N4 (graphitic/amide), and N5 (graphitic). Samples implanted at moderate doses (20–60 min) show very similar distributions of nitrogen species. Increasing the implantation time to 120 min further increases the N1, N2, and N4 peaks, implying a relative increase in the level of imide, pyridinic, graphitic and possibly amide groups, while amine-based nitrogen appears to reach a saturation limit after moderate dosages and perhaps converts to amide at longer dosages.

Implantation current series: Vulcan

To further understand the effects of implantation, the beam current was varied while maintaining a constant implantation time of 60 min. It was observed that a progressive increase in the beam current leads to a gradual increase in nitrogen content. At the highest beam currents, a 2x greater increase in nitrogen content is achieved compared with the time-variant implantation studies (Fig. 5A).

The changes in XPS and NEXAFS spectra associated with beam current variation are shown in Fig. 6. From this, it is clearly observed that Vulcan samples implanted in different dosage 'regimes' (low dose: 13/22mA; high dose 35/50mA) have dissimilar nitrogen

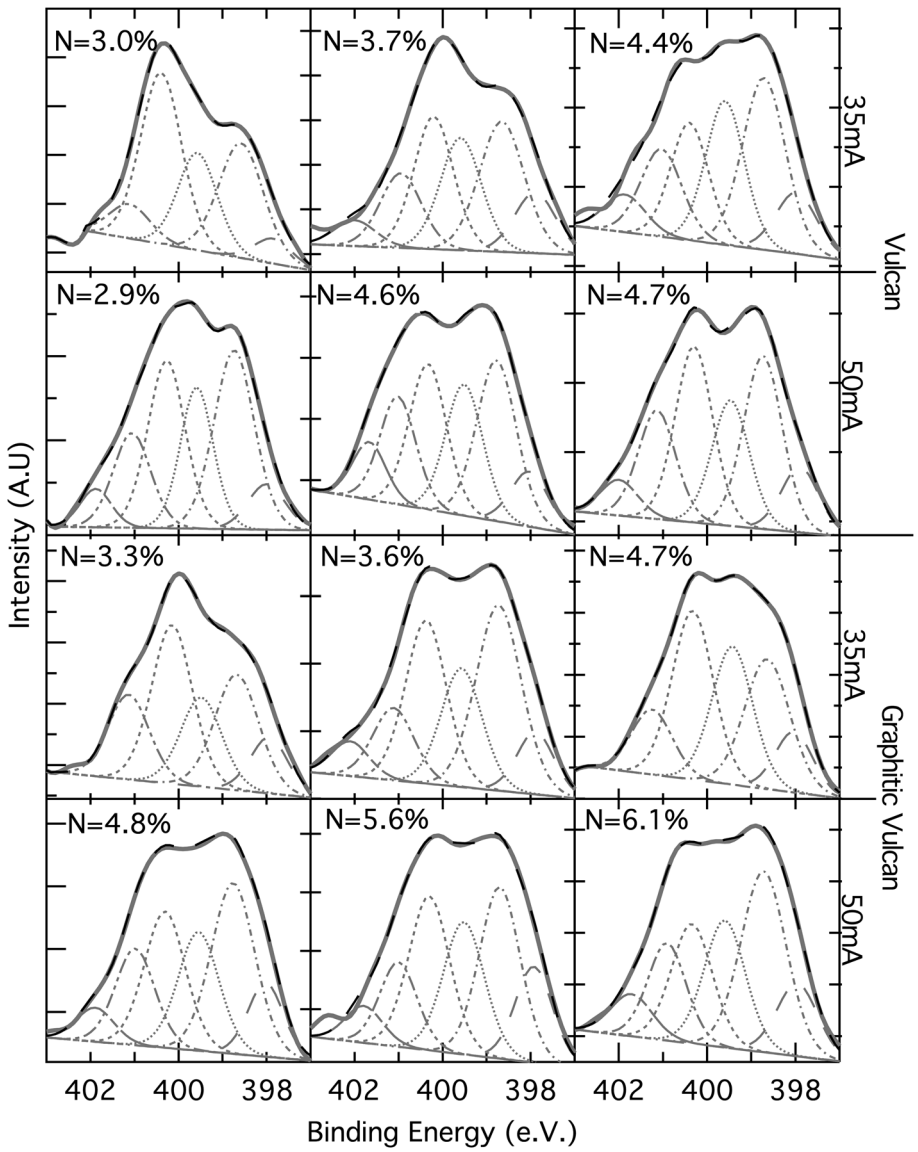

Figure 7. XPS high-resolution N1s spectra observed for the Vulcan and Graphitic Vulcan implanted for 60 min at beam currents of approximately 35 mA and 50 mA. Three areas per sample are shown to demonstrate variations in the nitrogen concentration and functionalities. Samples implanted at 50 mA tend to show more homogeneous distribution of nitrogen functionalities.

functionalities. As seen from XPS (Fig. 6A), samples implanted at the lowest dose condition (13 mA) show new nitrogen moieties, including graphitic and pyridinic species, similar to the time-series results discussed above. At slightly higher beam currents (22mA) a similar general shape of the N1s is observed, only with a slightly altered mix of graphitic, amide and pyridinic species (N5, N4, N2, respectively). In general, the N 1s XPS peak for both of these relatively "low dose" samples show a majority of species are centered near ~400 eV, with lower binding energy species being less abundant.

In the Vulcan samples implanted at 'high dose' conditions (35 mA and 50 mA), we observe a drastic increase in the amount of low-binding energy species that cause a broadening of the N1s spectra (Fig. 6 and 7). As previously discussed, the N2 peak (398.8 eV) is attributed to a pyridinic structure, where nitrogen in the aromatic ring is bound to two carbon atoms. Some samples implanted at these high conditions also show new peak at ~402 eV (N6), typically assigned to oxidized nitrogen groups, such as pyridine-N-oxide.[30] It is not surprising to detect these species in samples with the large amount of pyridinic N-species observed at 398.8 eV. The additional increase in low BE XPS species (below 398.5 eV) in these high-dose conditions could be due to imine groups and/or structures similar to those observed in triazine, heptazine and amorphous carbon nitride, indicative of high nitrogen defect densities (clustered, multi-nitrogen sites, Fig. 8).[45] All of these structures show XPS peaks at binding energies near N1. Additionally, the NEXAFS results (Fig. 6B) corroborate this possibility, as we observe the major signatures associated with those features increasing in intensity with increasing beam current. Specifically, the NEXAFS features at 398.9 eV and the 400 eV have been attributed to pure triazine[44] and polymers with triazine functionalities,[56] respectively. It is worth noting that peaks in this range (~398.5 eV and ~400 eV) have also been associated with porphyrin structures, which possess similar high concentrations of nitrogen sites. Therefore, we propose that XPS peaks at low-binding energies are a mix of single pyridnic nitrogen defects and multi-clustered nitrogen defects (e.g. triazine-like), similar to the structures shown in Fig. 8. According to previous experimental observations and DFT calculations, these types of clustered multi-nitrogen defects lead to enhanced catalyst-support interactions.[22]

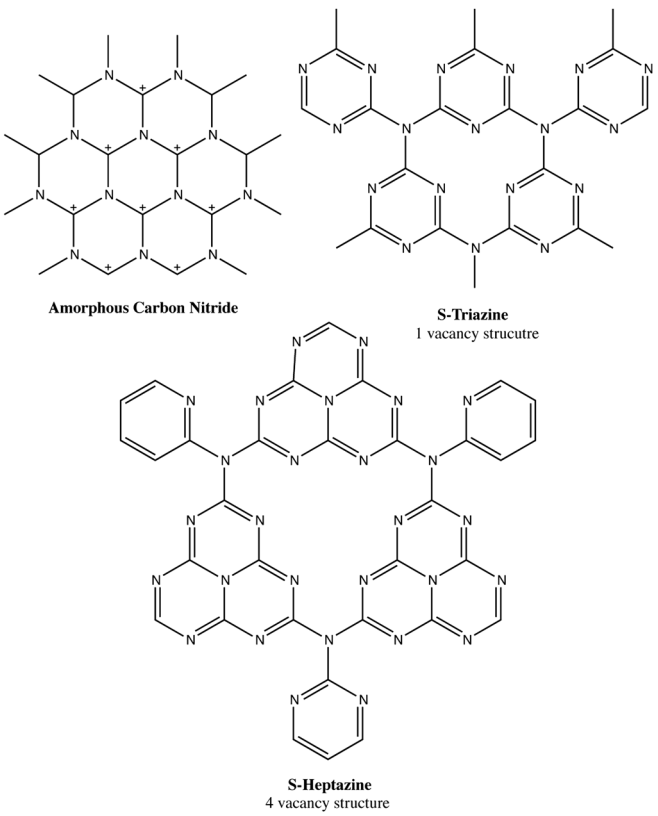

Figure 8. CN structures proposed for materials implanted at high dosages.

Implantation current series: Graphitic Vulcan

In addition to the Vulcan black, we also examined a series of modified Graphitic Vulcan samples. Fig. 5B demonstrates that the trend for the nitrogen content as a function of beam current for Graphitic Vulcan is the same as for Vulcan samples.

A small amount of nitrogen is detected in the unmodified Graphitic Vulcan, centered at N4 (400.3 eV) (Fig. 2B). This indicates that nitrogen in unmodified Graphitic Vulcan is most likely present as amide groups or graphitic nitrogen. The nature of the initial nitrogen species is thus very different between the unmodified Vulcan and Graphitic Vulcan materials. After implantation, the change in shape of the N1s spectra for Graphitic Vulcan modified at 13 mA (Fig. 6) indicates the incorporation of a wide variety of nitrogen species. Similarly, to the implanted Vulcan series, we observe the formation of N1, N2, N3, N4 and N5 spectral features, however a larger relative abundance of low BE species is observed (Specifically N2). As Implantation dose is increased, these low BE species (N1, N2) continue to increase relative to the high BE species (N3, N4, N5).

From the NEXAFS data, it is clear that the feature associated with graphitic nitrogen (400.5 eV) disappears for the graphitic Vulcan samples in favor of the more clustered structures. It is hypothesized that because of the different properties of the support (Graphitic Vulcan vs Vulcan), less graphitic nitrogen is observed in NEXAFS, while XPS still detects species corresponding to substitutional nitrogen (N5). This suggests that *single* graphitic nitrogen substitutions are replaced with more complex defect sites because only the peaks associated with clustered nitrogen/triazine peaks (398.9 eV and 400.0 eV) are observed in NEXAFS. Indeed, the ratio of the NEXAFS feature at 398.9 eV (pure triazine) to that at 400 eV (related to triazine bonded to a carbon framework[56]) is greater for the 50 mA condition than at the 25 mA condition. This could indicate that the number of pure triazine-like sites increases as beam current increases, revealing a continued shift toward carbon nitride-like films at high-dose conditions. These facts combined with the increase in low BE XPS features indicate the possibility of more clustered nitrogen defects (pyridine or triazine) occurring during high-dose conditions. Fig. 7 provides further comparison of the XPS spectra from the two materials (Vulcan and Graphitic Vulcan) as a function of beam current and reveals that high implantation dosages (50 mA) lead to similar distributions of nitrogen functionalities for both Vulcan and Graphitic Vulcan (although total nitrogen concentrations can vary). However, at any low dose condition the variations between Graphitic Vulcan and Vulcan become markedly different with respect to surface functionality and concentration.

Interestingly, the shape of N1s spectra obtained for Vulcan and Graphitic Vulcan doped at 50 mA (Fig. 7) is very similar to those obtained for PEEK and MSN doped using low dosages (Fig. 2). Therefore, by tuning the dosage to the specific carbon material used, one can obtain a consistent blend of clustered multi-nitrogen functional groups on the surface of various carbon materials. These

types of moieties have been previously reported to provide the best catalyst-support interactions.

Conclusions

This work underscores the complexity of carbons doped with nitrogen and offers a pathway to tune the composition through nitrogen ion implantation. The results show that the relative percent of sp, sp^2, and sp^3-hybridized nitrogen sites as well as doping concentration can be controlled by ion implantation parameters. Specifically, high current implantation conditions offer saturated nitrogen concentration levels and provide higher relative percentages of clustered nitrogen functionalities. It is also shown that during the initial implantation process, a cleaning of the carbon surface may occur, decreasing chemisorbed oxygen and nitrogen species. After this initial phase, a steady increase in nitrogen and oxygen functional groups is observed as nitrogen is implanted into the carbon matrix and edge defects are created. The data presented herein also points toward evidence that at saturated nitrogen concentrations, carbon nitride-like structures (e.g. Triazine, heptazine, etc.) may be forming at the carbon surface. These surface species could serve multiple purposes in various applications: (i) an increase in electrochemical stability compared with standard carbon; (ii) greatly improved conductivity to facilitate charge transport; (iii) stronger catalyst-support interactions to enhance the activity of precious metal; and (iv) suppression of precious metal agglomeration occurring due to migration/coalescence and dissolution/reprecipitation across the carbon surface.

Acknowledgements

The work at CSM is supported by the Army Research Office under grant #W911NF-09-1-0528 and start-up funds from CSM. The work at NREL is supported by the U.S. Department of Energy EERE, FCT Program, under Contract No. DE-AC36-08-GO28308 with the National Renewable Energy Laboratory. The authors also acknowledge Electron Microscopy Laboratory at CSM and surface analysis facilities at NREL. NEXAFS analysis was carried out at the Stanford Synchrotron Radiation Lightsource, a Directorate of SLAC National Accelerator Laboratory and an Office of Science User Facility.

References

[1] K. Kinoshita, *Angew. Chemie Int. Ed. English* **1988**, *27*(9), 1218–1219.
[2] S. Maldonado, S. Morin, K. J. Stevenson, *Carbon N. Y.* **2006**, *44*(8), 1429–1437.
[3] D. Jana, C.-L. Sun, L.-C. Chen, K.-H. Chen, *Prog. Mater. Sci.* **2013**, *58*(5), 565–635.
[4] S. Maldonado, K. J. Stevenson, *J. Phys. Chem. B* **2005**, *109*(10), 4707–4716.
[5] P. Ayala, R. Arenal, M. Rümmeli, A. Rubio, T. Pichler, *Carbon N. Y* **2010**, *48* (3), 575–586.
[6] P. Barpanda, K. Djellab, R. K. Sadangi, A. K. Sahu, D. Roy, K. Sun, *Carbon N. Y* **2010**, *48*(14), 4178–4189.
[7] L. M. Malard, M. A. Pimenta, G. Dresselhaus, M. S. Dresselhaus, *Phys. Rep* **2009**, *473*(5–6), 51–87.
[8] H. Wang, R. Côté, G. Faubert, D. Guay, J. P. Dodelet, *J. Phys. Chem. B* **1999**, *103*(12), 2042–2049.
[9] F. Xu, M. Wang, Q. Liu, H. Sun, S. Simonson, N. Ogbeifun, E. A. Stach, J. Xie, *J. Electrochem. Soc.* **2010**, *157*(8), B1138.
[10] R. Borup, J. Meyers, B. Pivovar, Y. S. Kim, R. Mukundan, N. Garland, D. Myers, M. Wilson, F. Garzon, D. Wood, P. Zelenay, K. More, K. Stroh, T. Zawodzinski, J. Boncella, J. E. McGrath, M. Inaba, K. Miyatake, M. Hori, K. Ota, Z. Ogumi, S. Miyata, A. Nishikata, Z. Siroma, Y. Uchimoto, K. Yasuda, K.-I. Kimijima, N. Iwashita, *Chem. Rev.* **2007**, *107*(10), 3904–3951.
[11] K. N. Wood, S. Pylypenko, T. S. Olson, A. A. Dameron, K. O'Neill, S. T. Christensen, H. N. Dinh, T. Gennett, R. O'Hayre, K. O'Neill, R. O'Hayre, *ACS Appl. Mater. Interfaces* **2012**, *4*(12), 6728–6734.
[12] L. S. Panchakarla, A. Govindaraj, C. N. R. Rao, *Inorganica Chim. Acta* **2010**, *363*(15), 4163–4174.
[13] V. Strelko, V. Kuts, P. Thrower, *Carbon N. Y.* **2000**, *38*(10), 1499–1503.
[14] S. C. Roy, E. Siebert, A. Hammou, H. Tagawa, M. Katou, K. Hirano, K. J. Tsuneyoshi, *Electrochem. Soc* **1996**, *143*(10), 3073.
[15] K. N. Wood, R. O'Hayre, S. Pylypenko, *Energy Environ. Sci.* **2014**, *7*(4), 1212–1249.
[16] T. Maiyalagan, *Appl. Catal. B Environ* **2008**, *80*(3–4), 286–295.
[17] Y. Zhou, K. Neyerlin, T. S. Olson, S. Pylypenko, J. Bult, H. N. Dinh, T. Gennett, Z. Shao, R. O'Hayre, *Energy Environ. Sci* **2010**, *3*(10), 1437.
[18] S. Pylypenko, A. Queen, T. S. Olson, A. Dameron, K. O'Neill, K. C. Neyerlin, B. Pivovar, H. N. Dinh, D. S. Ginley, T. Gennett, R. O'Hayre, *J. Phys. Chem. C* **2011**, *115*(28), 13667–13675.
[19] K. N. Wood, S. T. Christensen, S. Pylypenko, T. S. Olson, A. A. Dameron, K. E. Hurst, H. N. Dinh, T. Gennett, R. O'Hayre, *MRS Commun.* **2012**, *2* (03), 85–89.
[20] Y. Shao, J. Sui, G. Yin, Y. Gao, *Appl. Catal. B Environ.* **2008**, *79*(1), 89–99.
[21] Y. Zhou, R. Pasquarelli, T. Holme, J. Berry, D. Ginley, R. O'Hayre, *J. Mater. Chem.* **2009**, *19*(42), 7830.
[22] S. Pylypenko, A. Borisevich, K. L. More, A. R. Corpuz, T. Holme, A. A. Dameron, T. S. Olson, H. N. Dinh, T. Gennett, R. O'Hayre, *Energy Environ. Sci.* **2013**, *6*(10), 2957.
[23] C. L. Muhich, J. Y. Westcott, T. C. Morris, A. W. Weimer, C. B. Musgrave, *J. Phys. Chem. C* **2013**, *117*(20), 10523–10535.
[24] J. D. Wiggins-Camacho, K. J. Stevenson, *J. Phys. Chem. C* **2011**, *115*(40), 20002–20010.
[25] K. Ghosh, M. Kumar, T. Maruyama, Y. Ando, *Carbon N. Y.* **2010**, *48*(1), 191–200.
[26] S. Pylypenko, A. Queen, T. S. Olson, A. Dameron, K. O'Neill, K. C. Neyerlin, B. Pivovar, H. N. Dinh, D. S. Ginley, T. Gennett, R. O'Hayre, *J. Phys. Chem. C* **2011**, *115*(28), 13676–13684.
[27] T. S. Olson, A. A. Dameron, K. N. Wood, S. Pylpenko, K. E. Hurst, S. Christensen, J. B. Bult, D. S. Ginley, R. O'Hayre, H. Dinh, T. Gennett, R. O'Hayre, *J. Electrochem. Soc.* **2013**, *160*(4), F389–F394.
[28] P. Joghee, S. Pylypenko, T. Olson, A. A. Dameron, A. R. Corpuz, H. N. N. Dinh, K. N. Wood, K. O'Neill, K. E. Hurst, G. Bender, K. J. O'Neill, T. Gennett, B. S. Pivovar, R. P. O'Hayre, *J. Electrochem. Soc.* **2012**, *159* (11), F768–F778.
[29] A. R. Corpuz, T. T. S. Olson, P. Joghee, S. Pylypenko, A. A. A. A. Dameron, H. N. H. N. Dinh, K. J. K. J. O'Neill, K. E. K. E. Hurst, G. Bender, T. Gennett, B. S. B. S. Pivovar, R. M. R. M. Richards, R. P. O'Hayre, *J. Power Sources* **2012**, *217*, 142–151.
[30] T. Susi, T. Pichler, P. Ayala, *Beilstein J. Nanotechnol.* **2015**, *177–192*.
[31] A. A. Dameron, T. S. Olson, S. T. Christensen, J. E. Leisch, K. E. Hurst, S. Pylypenko, J. B. Bult, D. S. Ginley, R. P. O. Hayre, H. N. Dinh, T. Gennett, R. P. O'Hayre, *ACS Catal.* **2011**, *1*(10), 1307–1315.
[32] I. Jiménez, A. F. Jankowski, L. J. Terminello, D. G. J. Sutherland, J. A. Carlisle, G. L. Doll, W. M. Tong, D. K. Shuh, F. Himpsel, *J. Phys. Rev. B* **1997**, *55*(18), 12025–12037.
[33] G. Beamson, *J. Chem. Educ.* **1993**, *70*(1), A25.
[34] M. J. Grunze, J. Fuhler, M. Neumann, C. R. Brundle, D. J. Auerbach, J. Behm, *Surface Science Letters.* **1984**, A122–A123.
[35] Z. Xiao, F. Peng, X. Li, R. Zhang, W. He, T. Zhou, *Surf. Interface Anal.* **2013**, *45*(13), 1869–1877.
[36] S. Barazzouk, C. Daneault, *Nanomaterials* **2012**, *2*(4), 187–205.
[37] N. Hellgren, J. Guo, Y. Luo, C. Såthe, A. Agui, S. Kashtanov, J. Nordgren, H. Ågren, J.-E. Sundgren, *Thin Solid Films* **2005**, *471*(1–2), 19–34.
[38] I. Shimoyama, G. Wu, T. Sekiguchi, Y. Baba, *Phys. Rev. B - Condens. Matter Mater. Phys* **2000**, *62*(10), 6053–6056.
[39] J. T. Titantah, D. Lamoen, *Diam. Relat. Mater.* **2007**, *16*(3), 581–588.
[40] K. Artyushkova, B. Kiefer, B. Halevi, A. Knop-Gericke, R. Schlogl, P. Atanassov, *Chem. Commun.* **2013**, *49*(25), 2539–2541.
[41] G. Wu, C. M. Johnston, N. H. Mack, K. Artyushkova, M. Ferrandon, M. Nelson, J. S. Lezama-Pacheco, S. D. Conradson, K. L. More, D. J. Myers, P. Zelenay, *J. Mater. Chem.* **2011**, *21*(30), 11392.
[42] H. T. Chung, C. M. Johnston, K. Artyushkova, M. Ferrandon, D. J. Myers, P. Zelenay, *Electrochem. Commun.* **2010**, *12*(12), 1792–1795.
[43] C. Jama, A. Al Khawwam, A.-S. Loir, P. Goudmand, O. Dessaux, L. Gengembre, J. Grimblot, *Surf. Interface Anal.* **2001**, *31*(9), 815–824.
[44] S. Trasobares, C. Kolczewski, R. Räty, N. Borglund, A. Bassan, G. Hug, C. Colliex, S. Csillag, L. G. M. Pettersson, *J. Phys. Chem. A* **2003**, *107*(2), 228–235.

[45] S. Kabir, K. Artyushkova, A. Serov, B. Kiefer, P. Atanassov, *Surf. Interface Anal.* **2016**, n/a–n/a.
[46] S. Kundu, T. C. Nagaiah, W. Xia, Y. Wang, S. V. Dommele, J. H. Bitter, M. Santa, G. Grundmeier, M. Bron, W. Schuhmann, M. Muhler, *J. Phys. Chem. C* **2009**, *113*(32), 14302–14310.
[47] W. Gammon, O. Kraft, A. Reilly, B. Holloway, *Carbon N. Y.* **2003**, *41*, 1917–1923.
[48] M. Mauerer, P. Zebisch, M. Weinelt, H.-P. Steinrück, *J. Chem. Phys.* **1993**, *99*(5), 3343.
[49] D. Duflot, C. Hannay, J.-P. Flament, M.-J. Hubin-Franskin, *J. Chem. Phys.* **1998**, *109*(13), 5308.
[50] R. Gago, I. Jiménez, J. Neidhardt, B. Abendroth, I. Caretti, L. Hultman, W. Möller, *Phys. Rev. B* **2005**, *71*(12), 125414.
[51] H. Niwa, K. Horiba, Y. Harada, M. Oshima, T. Ikeda, K. Terakura, J. I. Ozaki, S. Miyata, *J. Power Sources* **2009**, *187*(1), 93–97.
[52] J. M. Ripalda, E. Román, L. Galán, I. Montero, S. Lizzit, A. Baraldi, G. Comelli, G. Paolucci, A. Goldoni, *J. Chem. Phys.* **2003**, *118*(8), 3748.
[53] T. Schiros, D. Nordlund, L. Pálová, D. Prezzi, L. Zhao, K. S. Kim, U. Wurstbauer, C. Gutiérrez, D. Delongchamp, C. Jaye, D. Fischer, H. Ogasawara, L. G. M. Pettersson, D. R. Reichman, P. Kim, M. S. Hybertsen, A. N. Pasupathy, *Nano Lett.* **2012**, *12*(8), 4025–4031.
[54] L. Lai, H. Yang, L. Wang, B. K. Teh, J. Zhong, H. Chou, L. Chen, W. Chen, Z. Shen, R. S. Ruoff, J. Lin, *ACS Nano* **2012**, *6*(7), 5941–5951.
[55] S. T. Christensen, D. Nordlund, T. Olson, K. E. Hurst, A. A. Dameron, K. J. O'Neill, J. B. Bult, H. N. Dinh, T. Gennett, *J. Mater. Chem. A* **2016**, *4* (2), 443–450.
[56] A. Fujimori, N. Sato, K. Kanai, Y. Ouchi, K. Seki, *Langmuir* **2009**, *25*(2), 1112–1121.

Supporting Information

Additional supporting information may be found in the online version of this article at the publisher's web site.

Figure SI 1. Raman analysis of N-doped carbons.
Figure SI 2. Representative SEM images of carbon materials.